Accepted Manuscript

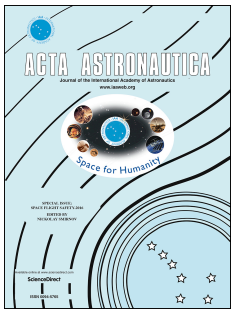

Numerical study of a novel monolithic heat exchanger for electrothermal space propulsion

F. Romei, A. Grubisic

PII: S0094-5765(18)31518-2

DOI: https://doi.org/10.1016/j.actaastro.2019.03.025

Reference: AA 7375

To appear in: *Acta Astronautica*

Received Date: 10 September 2018

Revised Date: 24 December 2018

Accepted Date: 8 March 2019

Please cite this article as: F. Romei, A. Grubisic, Numerical study of a novel monolithic heat exchanger for electrothermal space propulsion, *Acta Astronautica* (2019), doi: https://doi.org/10.1016/j.actaastro.2019.03.025.

Numerical Study of a Novel Monolithic Heat Exchanger for Electrothermal Space Propulsion

F. Romei* and A. Grubisic
University of Southampton, Southampton, SO17 1BJ, UK

Abstract

Fully-coupled multiphysics simulations are applied to investigate a number of candidate heat exchanger materials in the Super-High Temperature Additively-Manufactured Resistojet (STAR) thruster. Two mission applications are considered: a low earth orbit (LEO) primary propulsion application and a secondary reaction control system (RCS) application of an all-electric geostationary (GEO) telecommunications platform. High-temperature operation provides a significant increase in specific impulse over the state-of-the-art Xenon-resistojets. Inconel 718 is investigated for moderate-performance for LEO applications, while pure tantalum and pure rhenium are examined for the extreme temperature high-performance GEO application. Simulations determine the attainable performance including heat transfer, Navier-Stokes continuum flow and Joule heating physics in both transient and steady state. Nozzle efficiency, heat exchanger efficiency, electrical characteristics and other key performance indicators are explored.

Keywords: Electrothermal Propulsion; Additive Manufacturing; Geometrical Arrangements Design; High Temperature; Refractory metals.

1. Introduction

Electric spacecraft propulsion has been in development since the 1960s, with numerous high-value telecommunications satellites now carrying electric propulsion, performing combined electric orbit raising and station-keeping functions. This combined application has been termed all-electric and presents a highly mass efficient solution for telecoms spacecraft. A new possibility has emerged for geostationary (GEO) platforms, whereby all-electric systems is augmented by utilising high-temperature xenon (Xe) resistojets for the reaction control system (RCS) [1]. On all-electric spacecraft, RCS systems still require hazardous hydrazine propellant in a separate independent secondary propulsion system, presenting significant cost increase and integration complexity. A xenon resistojet, operating in parallel with an all-electric system from a common propellant, would remove the requirement for hydrazine systems [2]. Furthermore, high-temperature xenon resistojets could improve the existing performance of state-of-the-art Xe resistojet thrusters used as primary propulsion for low earth orbit (LEO) spacecraft [3, 4].

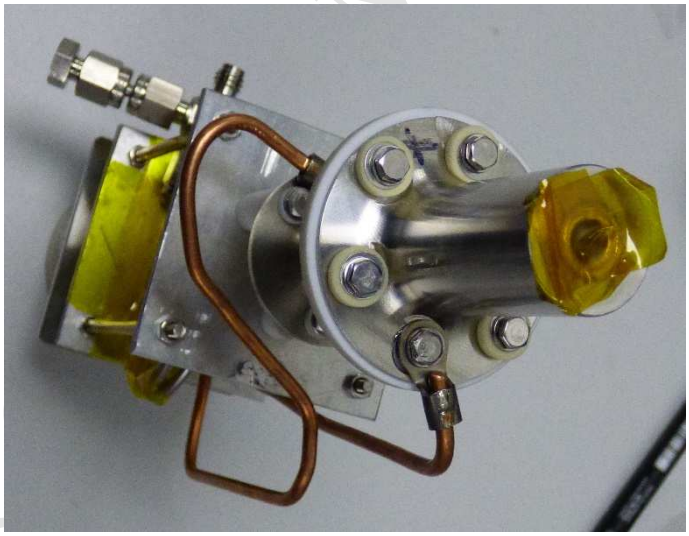

Fig. 1. STAR prototype thruster in 316L stainless steel.

Electrothermal heating augmentation provides a significant improvement in performance with respect to cold gas propulsion systems. However, to facilitate GEO mission applications a significant increase in performance is required over existing state-of-the-art resistojets [5]. The Super-high Temperature Additive Resistojet (STAR) meets these requirements by utilising a novel regenerative monolithic heat exchanger manufactured by Selective Laser Melting (SLM). A proof-of-concept thruster made of 316L stainless steel has been successfully tested in high vacuum with argon propellant [6, 7] (Fig. 1). Whilst this material allows only a limited operational gas temperature for validation, high-temperature materials are necessary to build a high-performance

*Corresponding author.
E-mail address: f.romei@soton.ac.uk

Submitted to Acta Astronautica 9 September 2018

STAR engineering model. A tantalum heat exchanger has been successfully produced via SLM, with the same geometry of the 316L prototype [8]. This latter result shows that the STAR thruster geometry is achievable with this material and provides a baseline for further investigations using other refractory metals in pure metals or alloys.

1.1 Super-high Temperature Additive Resistojet Description

An electrothermal thruster accelerates the propellant gas thermodynamically. Therefore, the higher the gas temperature and pressure, the higher is the exhaust velocity. In order to understand the physical phenomenon, let us consider the simplest model of an electrothermal thruster with the following assumptions: (1) a one-dimensional flow; (2) constant specific heats; (3) the electrical power, $P_{??}$, is transferred to the gas with 100% thermal efficiency, with the propellant gas reaching a final stagnation temperature, $??_0$, equal to the chamber temperature, $??_{??}$. The gas stream is accelerated through a de Laval nozzle, where the static temperature decreases to $??_{??}$ at the nozzle exit. If the total enthalpy $□_0$ is conserved along the thruster axis, such as the process is adiabatic, then the total enthalpy is given by Eq.(1), where for an ideal gas $□ = ??_{??}??$, with $??_{??}$ the gas constant pressure specific heat per unit mass. Therefore, the total enthalpy will be equal both in the thruster chamber (??) and in the nozzle exit plane (??). It is also convenient to assume that $??_{??} \ll ??_{??}$ and $??_{??} \gg ??_{??}$ and obtain the relation given by Eq.(2) [9]. The specific impulse, I_{sp}, is the main thruster performance parameter expressed in seconds through Eq.(3) where η_n is the nozzle efficiency, T_0 is the stagnation temperature at the nozzle inlet and g_0 the sea-level gravitational acceleration. Specific impulse is related to the exit velocity, v_e, of the propellant. A high-temperature resistojet maximises the stagnation temperature, therefore the specific impulse.

$$h_0 = h_c + \frac{u_c^2}{2} = h_e + \frac{u_e^2}{2} \tag{1}$$

$$\frac{u_e^2}{2} = \frac{u_c^2}{2} + c_p(T_c - T_e) \gg c_p T_c \tag{2}$$

$$I_{sp} = \frac{v_e}{g_0} \gg h_n \sqrt{2 c_p T_0} \,/\, g_0 \tag{3}$$

1.1.1 Materials selection

In the current research, SLM has been used to produce the first additively manufactured resistojet with a monolithic regenerative exchanger (Fig. 2). This consists of four thin-wall tubes, connected to form an electrical resistance path, in which power is dissipated when a potential is applied. The heat exchanger component also includes an integrated converging-diverging nozzle. The first prototype of the STAR thruster, in 316L stainless steel, can operate in the region of 1100 K depending on the mechanical load and environmental conditions. The STAR geometrical design has been developed to be used with high-temperature materials to obtain a gas temperature in the region of 2500 K.

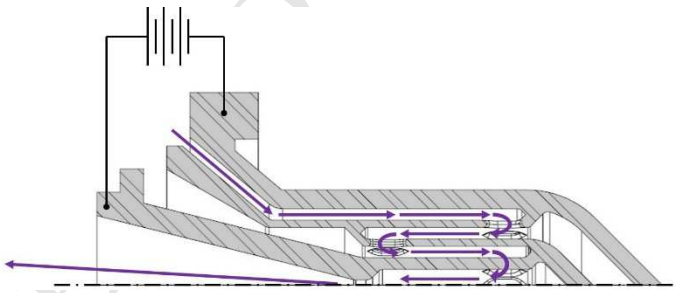

Fig. 2. Axial-symmetric schematics of the STAR monolithic heat exchanger concept. The xenon flow path (purple) and the electrical interface are shown [5].

In the literature, the resistojet heat exchanger design shown to provide the highest overall efficiency for the highest gas temperature is the concentric regenerative type [10-12]. In this design, the resistive heating elements also form the flow channels, which results in direct heating of the propellant. For these reasons, the maximum gas temperature is close the maximum structural temperature of the thruster. In past research studies, with hydrogen propellant, the design offered an overall efficiency of 79% with an electrical power of 3 kW, reaching a gas temperature in the range 2400 – 2500 K [13, 14].

The only materials capable of both reaching the temperature and thus performance requirement of the STAR thruster that can also form an electrical heater are refractory metals and their alloys. By definition, refractory metals have a melting point higher than 1800°C and are characterised by high hardness at room temperature [15]. Commonly, the refractory metals consist of niobium (Nb), molybdenum (Mo), tantalum (Ta), tungsten (W) and rhenium (Re). The only pure materials able to work in the region of 3,000K are Ta, W, Re and Os. Os oxide is volatile and extremely toxic, therefore it is rarely used in its pure state, and it is instead often alloyed with other metals.

Table 1 shows a comparison between four candidate materials for the STAR application: Inconel 718 and pure Ta, Re and W. Parameters for comparison are the melting range of the materials, T_{melt}, the maximum operating temperature, MOT, the attainable specific impulse, I_{sp}, and the hot to cold specific impulse gain, $\hat{I}_{sp}$. The specific impulse is calculated using Eq.(3) with the

assumptions of T_0 = MOT and η_n = 90%. Fig. 3 depicts $\hat{I}_{sp}$ as a function of the stagnation temperature calculated using Eq.(4), which can be obtained with the ratio of specific impulse calculated in the cold gas (300K) and in the hot gas cases.

Table 1: Comparison between candidate materials and attainable performance.

Parameter	Units	Inconel 718	Tantalum	Rhenium	Tungsten
T_{melt}	K	1533 - 1609	3290	3459	3700
MOT	K	1350	2640	2800	2960
I_{sp}	s	60	84	86	89
$\hat{I}_{sp}$	%	+53	+66	+67	+68

$$\hat{I}_{sp} = 1 - \frac{\sqrt{300K}}{\sqrt{T_0}} \tag{4}$$

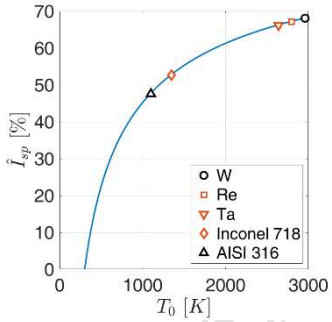

Fig. 3. Specific impulse gain with increasing stagnation temperature. The materials in analysis are highlighted in orange

Fig. 4 shows the electrical resistance of Inconel 718 [16], Stainless Steel 316 [17], Rhenium [solid,annealed] (from COMSOL material library), Tantalum and Tungsten with purity above 99.9% and 99.99% respectively [18]. Inconel alloys are high-strength and corrosion resistant nickel-chromium materials used commonly up to 1000 K. However, they can operate at temperatures as high as 1350 K depending on the ambient and load conditions. Whilst this material can only develop up to 60 s specific impulse with the above assumptions, the increased electrical resistivity is attractive for the development of a high performance thruster LEO applications. In particular, a higher resistance would result in a reasonable supply voltage for a given power, which is more convenient from a power supply perspective. In addition, the resistivity of Inconel is quasi-constant with a cold-to-hot ratio of 93%, while for Re, Ta and W it is of 16%, 13% and 6% respectively (Fig. 4). The high ratio avoids a current peak load at cold thruster ignition if operating at constant voltage. Finally, Inconel is compatible with iodine propellant [19], which is a promising alternative propellant to Xe for the future of electric propulsion [20, 21].

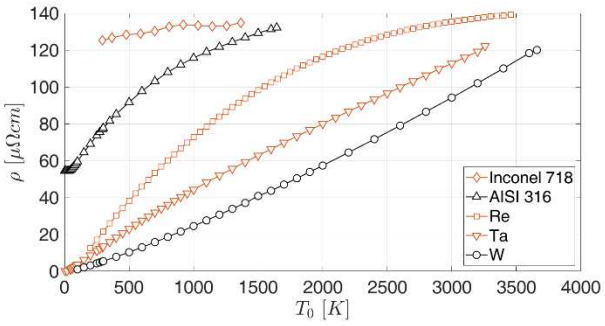

Fig. 4. Electrical resistivity of selected materials for the STAR resistojet heater. The materials in analysis are highlighted in orange.

Pure Ta, Re and W, are the highest melting point refractory metals available, therefore attractive for the STAR application. Whilst W has the highest melting point among the others, it also has a high ductile-brittle transition temperature, in particular after heating above 2270 K, and also has a tendency to crack during welding [22]. For this reason, pure W is elimination as a heat

exchanger material choice. Pure Re does not present these issues and has been successfully demonstrated at 2500 K with hydrogen propellant [13, 14]. Ta is another suitable material with similar operational temperature, which has excellent resistance to corrosion and heat. Its implementation to the STAR thruster is currently in development, and the most critical component of the monolithic heat exchanger has been printed successfully in Ta with selective laser melting [8].

With respect to W, which is accessible at a relatively low price, Ta is an order of magnitude more costly, whilst the cost of Re is one further order of magnitude. While the current numerical study considers pure Ta and Re, ultimately the STAR heat exchanger material will be in an alloy of refractory metals. In particular, commercially available alloys of interest are TaW, TaNb MoRe and WRe. The latter is of significant interest as Re transfers its higher electrical resistivity in alloys of W (Fig. 4), which is more suitable for the STAR.

In general, resistojet materials selection is also based on appropriate testing in a relevant environment. It should be noted that the maximum structural temperature of any material depends on the mechanical load and on the ambient conditions. The resistojet is exposed to the vacuum space environment, or to pressurised inert monoatomic xenon. Xe used in electric propulsion has typically a purity of 99.9995%, with a maximum impurity of 0.1 PPM. Finally, the only load during operation is determined by the degree of thermal stress that the heating generates. For these reasons, the maximum structural temperatures selected are only an initial approximation to serve as a base of the investigation conducted in this paper.

1.1.2 Mission Requirements

The design priority for the STAR thruster is to increase the stagnation temperature of the propellant to the maximum possible level, therefore increasing fuel efficiency. The thruster requirements are defined by two missions scenarios, which would benefit from the STAR thruster [5]. Table 2 shows the requirements on the maximum expected operating pressure (MEOP), the thrust range, the average electrical power and the start-up duration, which is the maximum allowable time in which the thruster shall reach steady state operation in full working temperature.

In this analysis, Inconel has been selected for the small LEO platform scenario, due to compatibility with power requirements while provided reasonable specific impulse improvement with respect to the current available Xe-resistojets. Ta and Re are selected instead for the GEO platform scenario. The three thrusters are named STAR-Inc, Star-Ta and STAR-Re respectively.

Table 2. Resistojet requirements for two selected missions with Xe propellant.

Parameter	M1: Small LEO platform	M2: GEO platform
MEOP, bar	4	4
Thrust range, mN	20 – 50	50 – 500
Average power, W	< 50	< 500
Start-up duration, s	< 60	< 60

1.2 Methodology

The methodology of investigation is summarized in Table 3. The dimensioning of the thruster for the three cases in analysis (STAR-Inc, STAR-Ta and STAR-Re), begin with the dimensioning of the nozzle throat. Firstly, 1-D equations are used in step 1 to provide the throat radius and an initial estimate of the Reynolds number at the throat, which determines the flow regime within the nozzle. The throat radius is an input for the CFD-optimisation (step 2), which determines the optimum diverging nozzle angle, α_{opt}, maximising the specific impulse for a given stagnation condition. In this step, the nozzle efficiency, η_n, is calculated and serves as a baseline for the specific impulse determination in the following steps. The obtained nozzle geometry provides a computed mass flow rate, which is used for the following simulations of the full thruster. In step 3, the influence of the thermal insulation and of the radiation shielding are discussed. In addition, a stationary solver is used to define the electrical current necessary to reach the MOT of the respective materials (step 4). In step 5, a time-dependent study is used to depict the heating time of the thruster at constant current. Finally, a heating cycle example is shown for STAR-Inc. The multiphysics simulations are made with the software COMSOL Multiphysics 5.3 (Build: 260). Where not otherwise specified, the settings of materials, physics modules and solvers use default parameters.

Table 3. Summary of the study steps performed on the three cases under examination.

Description	Input	Output
1-D de Laval nozzle, adiabatic wall, constant specific heat expansion		
1) Nozzle dimensioning	$p_0, T_0 = T_m, F_d$	$r_t, \mathrm{Re}_t, I_{sp}$
2-D axis-symmetric, adiabatic wall, RANS k-ε turbulent model		
2) Nozzle CFD-optimisation	$r_t, p_0, T_0 = T_m$	$a_{opt}, F, I_{sp}, \dot{m}, h_n$
2-D axis-symmetric, laminar flow, stationary		
3) Insulation and radiation shielding assessment	$\dot{m}, p_0, I_{test}$	N_s , insulation
4) Find the current to reach MOT in infinite time	$\dot{m}, p_0, I_0, N_s$, insulation	$I_{stat} (T_m = \mathrm{MOT})$
2-D axis-symmetric, laminar flow, time-dependent		
5) Find the heating time at different currents	Initial condition = cold stationary solution	$t_h(I_1, ..., I_4)$
6) Heating cycle example of STAR-Inc	$\dot{m}, p_0, I_{cycle}$	$T_0(t), T_m(t), D(I_{test})$

2. STAR Nozzle Study

In this section, the nozzle is dimensioned to meet the requirements of thrust at the MEOP. At the same time, the nozzle diverging angle is optimised to maximise the specific impulse at given stagnation conditions. Firstly, the mass flow rate is estimated using Eq.(5), with the specific impulse calculated at the MOT of each respective material (Table 1) and using the required thrust for each mission with a 5% margin (Table 2). In the assumptions of a 1-D de Laval nozzle, adiabatic wall, constant specific heat expansion, the mass flow rate through the nozzle can be expressed by imposing the mass flow chocking condition (Mach = 1), which leads to Eq.(6), where A_t is the throat area and γ the specific heat ratio. This relation is used to calculate the throat radius at the given stagnation condition. The Reynolds number is evaluated at the throat to evaluate the flow regime using Eq.(7), where the dynamic viscosity of Xe is expressed as a fourth order polynomial valid up to 3000 K [23].

$$I_{sp} = \frac{F}{\dot{m} g_0} \tag{5}$$

$$\dot{m} = \frac{A_t p_0}{\sqrt{T_0}} \sqrt{\frac{g}{R}} \left(\frac{g+1}{2} \right)^{\frac{g+1}{2(g-1)}} \tag{6}$$

$$\mathrm{Re}_t = \frac{4\dot{m}}{\pi \mu D_t} \tag{7}$$

Fig. 5 shows the design regions corresponding to the two missions M1 and M2, where the calculated throat radiuses guarantee a working pressure corresponding to the MEOP at the maximum thrust level. While a smaller throat would not generate a sufficient thrust at the MEOP, a larger throat would decrease Reynolds number. The dashed iso-Reynolds lines indicate the laminar-turbulent transition for a pipe flow (Re = 2100 – 4000).

Resistojets usually generate a relatively low thrust level and are designed to operate at low chamber pressures with small throat dimensions. For these reasons, the Reynolds number can be low and the viscous losses significant. This effect can be mitigated by shortening the nozzle and by increasing the divergence angle [24]. For Reynolds numbers below the transition zone, the viscous effect becomes relevant and can significantly lower the nozzle efficiency [25, 26]. This has been proven experimentally for different nozzle shapes [27]. For this reason, a high-temperature STAR using Ta, Re or W is not desirable for M1, as the resulting Reynolds number falls in the laminar region over the whole range of thrust (20 – 50 mN). This issue is not present for M2. Therefore, the analysis is restricted to STAR-Inc on the M1 LEO requirements and to STAR-Ta and STAR-Re on the M2 GEO requirements.

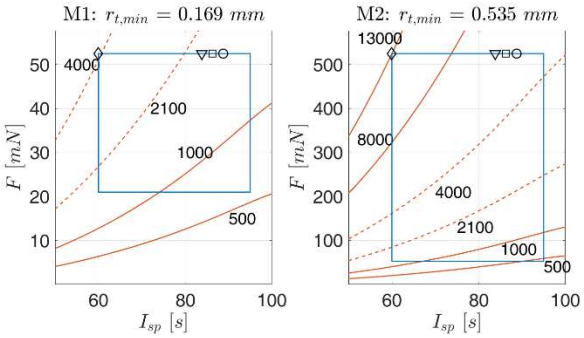

Fig. 5. Flow regime estimation with design box (in blue) in the (Isp, F) plane for the two missions M1 (left) and M2 (right). Iso-Reynolds lines indicate the nozzle flow regime, where the dashed-delimited area corresponds to the laminar-turbulent transition. Markers locate the maximum specific impulse attainable using Inconel 718 (diamond), Ta (triangle), Re (square) and W (circle).

2.1 CFD-optimisation

The nozzle has a fixed inlet to throat area ratio of 10, and a fixed outlet to throat area ratio of 200. The internal geometry is smoothed with fillets of the same radius as the throat. The converging angle if of 45°, while the diverging angle, α, is the parameter to optimise. The selection of the nozzle diverging angle, α, is a trade-off between the influence of viscosity on the nozzle wall, and the divergence of the flow. A CFD-optimization coupled method is performed to determine the optimum diverging angle, given the stagnation conditions, which maximises the specific impulse.

The model solves full N-S equations of a compressible flow, assuming a 2D axis-symmetric geometry and an adiabatic wall. The compressible Navier-Stokes (N-S) equations in the vectorial form are conservation of momentum, Eq.(8) of mass, Eq.(9), and of energy, Eq.(10).

$$r(\mathbf{u}\cdot\nabla)\mathbf{u} = \nabla\cdot[-p\mathbf{I} + \mu(\nabla\mathbf{u} + (\nabla\mathbf{u})^T) - 2/3\mu(\nabla\cdot\mathbf{u})\mathbf{I}] + \mathbf{F} \quad (8)$$

$$\nabla\cdot(r\mathbf{u}) = 0 \quad (9)$$

$$rC_p(\mathbf{u}\cdot\nabla)T = \nabla\cdot(k\nabla T) + Q + Q_{vh} + W_p \quad (10)$$

Where $\mathbf{u}$ is the velocity vector, Q_{vh} is the viscous heat, W_p is the pressure work, Q contains the heat source and F is the volume force. In this case, $Q = F = 0$. The High Mach Number Flow (HMNF) interface is used assuming a turbulent flow, which is modelled with the standard k − ε model and the built-in Kays-Crawford heat transport turbulence model [28]. At the inlet, stagnation pressure and temperature, and turbulence variables are defined. For a fully developed pipe flow, the turbulence intensity, I_T, and the turbulence length scale, L_T, are expressed by Eq.(11) and (12) respectively, where D_h represent the hydraulic diameter of the nozzle inlet. At the outlet, the boundary condition is defined as static pressure p = 0 bar.

$$I_T = 0.16\,\mathrm{Re}_{D_h}^{-1/8} \quad (11)$$

$$L_T = 0.038 D_h \quad (12)$$

The gradient-free Nelder-Mead optimization solver is used to maximise the objective function, J, which is equal to the specific impulse calculated with Eq.(5), where the mass flow rate and the thrust are defined at the nozzle exit plane through Eq.(13) and Eq.(14) respectively. These variables are the static temperature and pressure, and the radial and axial components of the velocity respectively.

$$\dot{m} = \int_0^{2\pi}\int_0^{r_e} \rho w\, dr\, dJ \quad (13)$$

$$F = \int_0^{2\pi}\int_0^{r_e} (\rho w^2 + p)\, dr\, dJ \quad (14)$$

2.2 Computational Grid Convergence

A structured computation mesh is parametrized as a function of a refinement parameter f, which is used for the mesh convergence analysis (Fig. 6). Both the number of radial elements and the number of axial elements are proportional to f. The discretization is refined close to the nozzle wall, i.e. where the boundary layer is located. In particular, the radial elements have an element ratio of 5 (ratio between the first and last radial length) with arithmetic progression. The number of quadrilateral elements if of 185 when f = 1, 4450 when f = 5 and 17700 when f = 10. The refinement parameter selected is f = 5, which corresponds to a relative error with respect to the finest solution below 0.5% for mass flow rate and thrust calculated as integral at the exit plane (Eq.(13) and (14) respectively). The relative error for T, p, u and w, calculated as average at the exit plane, falls below 5%.

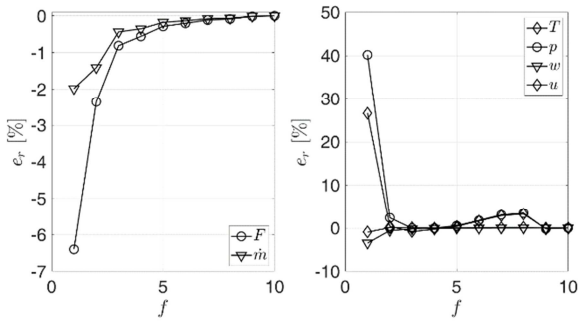

Fig. 6. Relative error of variables measured at the exit plane of the nozzle as a function of the mesh refinement parameter.

2.3 Results

Fig. 7 shows the optimisation results in terms of nozzle efficiency, defined as the ratio between the computed and the theoretical specific impulse, where the latter is given by Eq.(3) with η_n = 1. Table 4 summarises the results of the optimisation process in terms of nozzle optimum diverging angle, α_{opt}, theoretical mass flow rate from Eq.(6), computed mass flow rate, thrust, specific impulse and Reynolds number evaluated at the throat using Eq.(7) with average temperature and dynamic viscosity. It can be noted that the optimum angles are similar. This is not surprising since it is strongly dependant on the Reynolds numbers, which are also similar as previously discussed.

The calculation of the thrust using Eq.(14), hence specific impulse, is valid if the pressure term is sufficiently small when compared to the total thrust. If the pressure term is significant, the nozzle operates in a strong under-expanded mode. In this case, the streamlines at the exit of the nozzle are subjected to greater divergence loss, which results in a lower specific impulse. This effect cannot be evaluated with the geometrical assumption of the current model of a truncated nozzle at the exit. All three cases analysed are within the model validity, since the pressure term represents approximately 0.5% of the total thrust, which suggests that 99.5% of thrust is due to momentum.

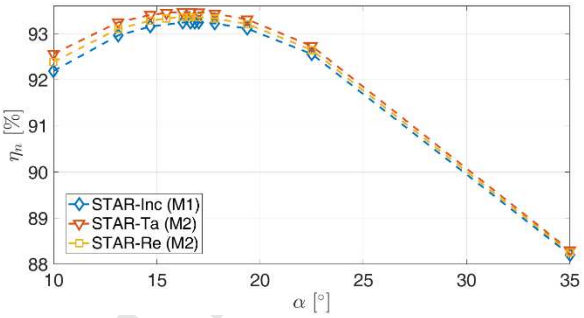

Fig. 7. Specific impulse efficiency optimisation for the three cases in analysis, as a function of the diverging angle of the nozzle.

Table 4. Results of the nozzle optimization for the three thrusters in analysis.

Parameter	STAR-Inc (M1)	STAR-Ta (M2)	STAR-Re (M2)
T_0 , K	1350	2640	2800
r_t , mm	0.169	0.535	0.535
$\dot{m}_{est}$, mg/s	89.3	638.7	620.1
$\dot{m}$, mg/s	86.55	620.7	602.65
F , mN	52.8	530.5	529.8
I_{sp} , s	62.2	87.1	89.6
h_n , %	93.3	93.5	93.4
a_{opt} , °	16.64	16.25	16.45
Re_t	4028	5734	5349

3. Multiphysics Study of the STAR Thruster

In this section, the STAR thruster is modelled to evaluate the electrothermal solution of the whole heat exchanger in the three cases of STAR-Inc, STAR-Ta and STAR-Re.

3.1 Geometry and assumptions

The STAR high-temperature resistojet computational geometry is shown in Fig. 8. The propellant enters from the rear of the thruster (inlet) and flows through the annular outer shell of the body. At the point of the nozzle spacer, the flow is directed into the inner heat exchanger, composed of four thin-wall tubes. In order to increase thermal efficiency, heat transfer from the high-power-density inner four walls to the outer shell of the thruster which ultimately radiates heat to space is minimised. The STAR design, therefore, includes a vacuum jacket to insulate the inner heat exchanger. Furthermore, the design includes an optional radiative heat shield, made of thin foils, placed in a vacuum jacket to minimise the radiative heat transfer from the inner to the outer part of the heat exchanger. In addition, a thermal insulator further lowers the casing temperature to minimise the radiation to space. The casing is surrounded with a thin metal foil of low emissivity. The influence of the radiation shielding and of the thermal insulation is discussed in Section 3.3.1.

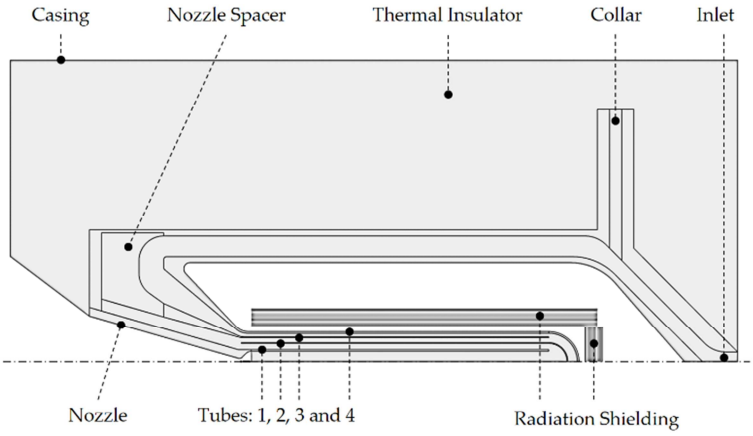

Fig. 8. 2-D axial symmetric geometry of the STAR thruster.

The four tubes of the heat exchanger have a thickness of 300 µm, 150 µm, 150 µm and 300 µm respectively in all simulations. This feature size is achievable with SLM and has been validated with the successful fabrication of the STAR-0 316L prototype and of the Ta heat exchanger. The length of the four tubes is set to two times the nozzle length, which follows from the nozzle dimensioning (Section 6). The resulting tubes length is of 15.5 mm for the STAR-Inc thruster and of 49 mm for the STAR-Ta and Re thrusters. The vacuum gap width is set to 1.5 times the nozzle outlet radius. The diameter of the thermal insulation is approximately equal to the full length of the thruster. The tungsten foil radiation shielding is 30 µm thick and wrapped within the vacuum jacket, at a distance of 1 mm from the inner heat exchanger walls and 0.2 mm between each layer.

A specific material is applied to each domain shown in Fig. 8. Where not indicated otherwise, these materials are available within the current version of the software. *Xenon [gas]* is used with modified dynamic viscosity and thermal conductivity (sourced from [23]) to extend their validity to 3000 K. *Inconel 718 [solid,full hardened]*, *Tantalum [solid]* and *Rhenium [solid,annealed]* are used respectively for the metal parts. *Tungsten [solid,Ho et al]* is used for the radiation shielding foils and for the casing external boundaries. In the case of STAR-Inc, the selected thermal insulator material is Promalight – 1200 [29], while for the other two thrusters is Denka Alcen [30]. The former is rated 1200°C made from an opacified blend of filament reinforced pyrogenic Al_2O_3, while the latter is rated 1600°C, composed of a polycrystalline wool fibre with Al_2O_3 (80%) and SiO_2 (20%).

For the thruster simulations, the nozzle flow is not solved. It is assumed that the heat transfer between the nozzle expansion area and the thruster body is negligible. Therefore, Eq. (8) to (10) are solved for weakly compressible flow, as such the density is evaluated at a reference pressure, $p_{ref} = p_0$, and is temperature dependent. The flow regime is assumed laminar for all the following simulations. Joule heating is modelled using the Electrical Currents (EC) interface, which is coupled with the HT interface to evaluate the heat source Q in Eq.(10). A constant current boundary condition is applied at one end of each tube, while at the other ends the grounding boundary condition is applied. The inlet boundary is set the mass flow rate resulted from the nozzle simulations (given in Table 4), while at the outlet boundary the stagnation pressure is defined, $p_0 = 4$ bar.

Surface to ambient radiation is applied over the whole exterior of the thruster, such as on the casing and the nozzle boundaries. For the nozzle surface, radiation to space is assumed a constant emissivity of 0.3 for Inconel. Surface-to-surface radiation is applied to the internal walls of the heat exchanger, assuming a constant emissivity of 0.6, which corresponds to the emissivity of the as-printed component.

3.2 Computational Grid Convergence

The computational grid convergence is conducted on the STAR-Ta thruster, without shielding nor thermal insulation. A free-triangular computation mesh is parametrized as a function of a refinement parameter *f*, which is used for the mesh convergence analysis (Fig. 9). The discretization is physics-controlled and corresponds to an extremely coarse mesh when $f = 1$, and to an extremely fine mesh when $f = 10$. The total number of elements is of 11121 when $f = 1$ and 63938 when $f = 10$. The selected mesh refinement parameter is f = 6, which guarantees e relative error to the finest computational grid of the selected variables within ±2%.

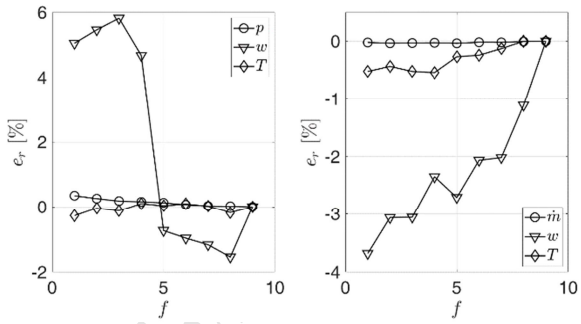

Fig. 9. Relative error calculated at the inlet (left) and at the outlet (right) of the heat exchanger.

3.3 Stationary Analysis

3.3.1 Insulation and Radiation Shielding Study

A stationary analysis of the model is used to quantify the effect of the thermal insulation and of the radiation shielding. Three test currents, obtained by trial and error, able to heat the thruster to nearly the MOT have been used in this analysis. Fig. 10 shows the STAR-Ta temperature distribution, depicting a significant increase of the gas temperature prior to the nozzle when including both the thermal insulation and the radiation shielding. Table 5 shows in detail the maximum temperatures achieved for both the structure, T_m, and for Xe at the nozzle inlet, T_0, for different amounts of radiation shield foils, N_s, where *shi* and *ins* indicate the presence (=1) or absence (=0) of the radiation shielding and of the insulator respectively.

The results show that STAR-Inc benefits significantly from the thermal insulation, providing a peak temperature increase of approximately 200 K, while negligible improvement is observed when including radiation shielding. On the other hand, the STAR-Ta and STAR-Re, benefit significantly from both the radiation shielding and from the thermal insulator due to significantly higher operating temperatures. When combined, they provide a greater increase in peak operating temperature than the sum of the two single cases. In fact, the radiation shielding is more effective at higher temperatures when using the thermal insulator.

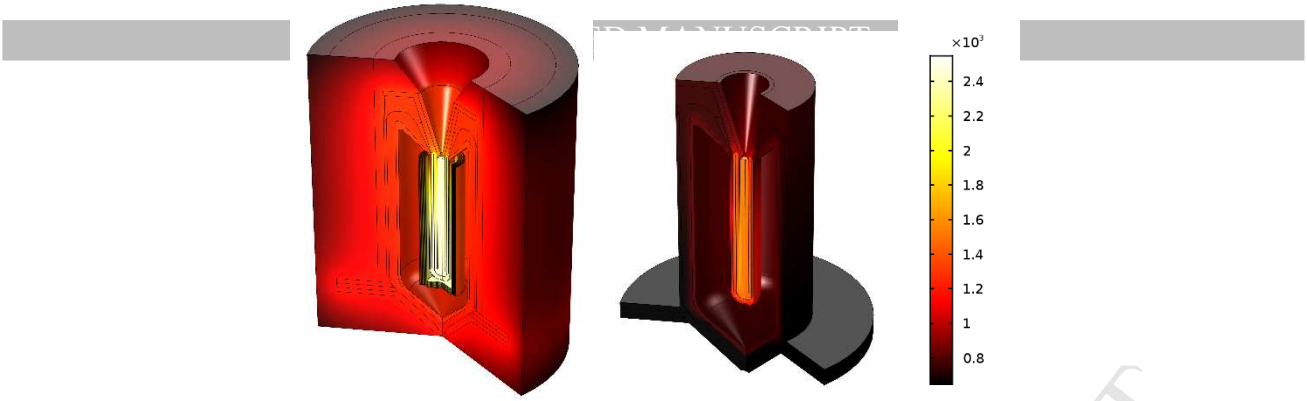

Fig. 10. Temperature stationary solution of STAR-Ta, at a test current of 77 A, showing the increase of maximum temperature when including both thermal insulation and radiation shielding located in the vacuum jacket.

Table 5. Summary of thermal insulation and radiation shielding parametrisation study.

Thruster	Var.	shi = 0 ins = 0	shi = 0 ins = 1	shi = 1 ins = 0	shi = 1 ins = 0	shi = 1 ins = 1	shi = 1 ins = 1
STAR-In I_{test} = 18*A*	T_m	1152	1371	1166	1166	1395	1395
	T_0	1014	1274	1030	1030	1299	1300
	N_s	-	-	5	10	5	10
STAR-Ta I_{test} = 75*A*	T_m	1670	1940	2146	2149	2550	2566
	T_0	1528	1842	1992	1995	2429	2444
	N_s	-	-	15	30	15	30
STAR-Re I_{test} = 70*A*	T_m	1668	1872	2068	2069	2324	2331
	T_0	1544	1773	1940	1941	2211	2217
	N_s	-	-	15	30	15	30

From the table above, the radiation shielding is considered fundamental for STAR-Ta and STAR-Re thrusters, while for STAR-Inc this can be eliminated, reducing the complexity of the assembly. The next series of studies are based on these selected configurations. For both extreme-temperature thrusters, the selected number of radiation shielding foils is 15, since the further increase in gas temperature using 30 foils is negligible and does not justify the additional weight and assembly complexity required.

3.3.2 Stationary Current Optimisation

The required electrical current necessary to heat the thruster up to the maximum structural temperature is obtained with a multiphysics-optimisation study. This uses the Nelder-Meads gradient-free algorithm, with the objective function expressed in Eq.(15) to be minimised, with an optimality tolerance of 0.01. The control parameter is the electrical current, with lower and upper bounds of 90% and 110% of the respective test currents used in Section 3.3.1. This study is fundamental to evaluate the ultimate stagnation temperature achievable, thus the maximum attainable specific impulse. The stationary current, I_{stat}, and other parameters are listed in Table 6. (16) are used to evaluate the heat exchanger efficiency, including η_h, expressed as the ratio of the stagnation gas power calculated at the inlet of the nozzle, P_0, and the total input power into the thruster, P_{ts}. The latter is the sum of the electrical power, P_e, and the stagnation power associated to the inlet gas, $P_{0,in}$. It has to be noted that the inlet gas temperature is not fixed as a boundary condition. In particular, no boundary conditions are applied at the back of the thruster. With this assumption, the thruster is perfectly isolated from the spacecraft, whereas in reality some heat would be transferred to the spacecraft by conduction through mechanical interfaces.

$$J = (T_m / \mathrm{MOT} - 1)^2 \times 10^3 \tag{15}$$

$$h_h = \frac{P_0}{P_{ts}} = \frac{P_0}{P_e + P_{0,in}} = \frac{\dot{m} c_p T_0}{V \times I + \dot{m} c_p T_{0,in}} \tag{16}$$

Parameter	STAR-Inc (M1)	STAR-Ta (M2)	STAR-Re (M2)
h_h [%]	66.5	62.2	59.0
T_0 [K]	1252.9	2424.6	2618.5
P_e [W]	13.3	277.6	310.8
I_{stat} [A]	17.6	77.0	75.5
$T_{0,in}$ [K]	944	1212	1282

Table 6. Summary of main thruster parameters in the stationary case when T_m = MOT.

3.4 Time-Dependent Analysis

3.4.1 Time to Operational Temperature

While I_{stat} is the current necessary to maintain in thermal equilibrium the thruster, the time necessary to reach such a condition can be long. The time necessary to reach the operational temperature is determined with a time-dependent simulation of the thruster ignition at four increasing current levels, beginning from I_{stat}. The stationary solution of the thruster in cold state is used as initial solution for the time-dependent solver. The current increases to the test value after 1 s and reaches the maximum value in 0.1 s. A stop condition, set into the time-dependent solver, ends each simulation when the maximum structural temperature, T_m, reaches the MOT. Fig. 11 shows the resulting temperature increase over time for the STAR-Inc. Due to the peculiar quasi-constant resistivity of Inconel (Fig. 4), the electrical power is almost constant in time at each one of the current levels analysed, and it corresponds to 13 W (at 120 s), 25.3 W, 37.3W and 49.3 W respectively. It can be noted that with I_{stat} the objective of reaching the MOT of Inconel is still far from achieved after 120 s of power application. In all the other three cases the objective is reached within the start-up requirement of 60 s.

Fig. 12 shows the temperature rising for STAR-Ta and STAR-Re. For the former, the electrical power evaluated at the last time step for each current is 158.6 W at 120 s, 349.6 W at 120 s, 438.4 W at 55.3 s and 512.4 W at 35.1 s. For the latter, the electrical power evaluated at the last time step for each current is 270.2 W at 120 s, 348.4 W at 120 s, 421 W at 108.2 s and 477.8 W at 51.1 s. In general, at lower currents, Re has the ability to heat faster than Ta due to higher electrical resistivity at low temperature (Fig. 4).

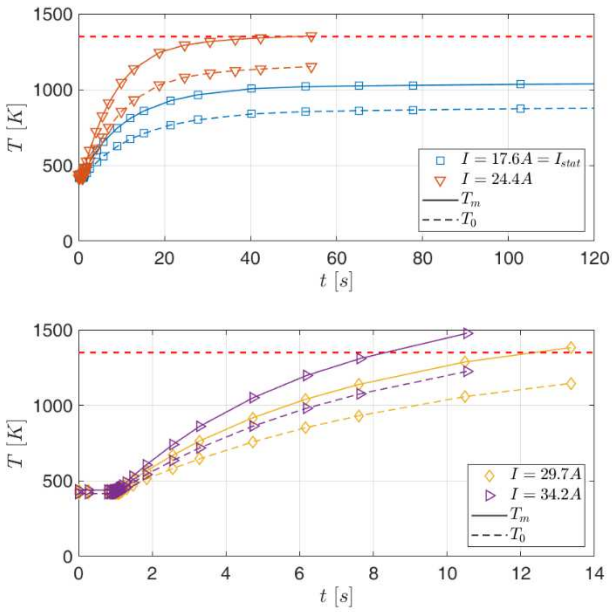

Fig. 11. Ignition of STAR-Inc from cold gas stationary solution. Maximum structural temperature (solid line) and Xe stagnation temperature at the inlet of the nozzle (dashed line) are shown at four current levels. The MOT of Inconel 718 is represented with a horizontal dashed line.

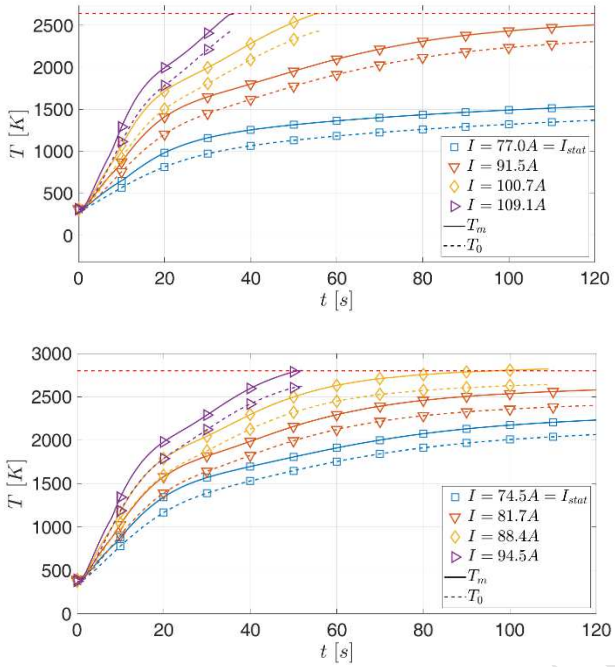

Fig. 12. Ignition of STAR-Ta (top) and of STAR-Re (bottom) from cold gas stationary solution. Maximum structural temperature (solid line) and Xe stagnation temperature at the inlet of the nozzle (dashed line) are shown at four current levels. The MOT of the two materials are represented with a horizontal dashed line.

3.4.2 Heating Cycle Example for STAR-Inc

The STAR thruster is characterized by a relatively low electrical resistance, requiring high-currents at low-voltage. A possible means of power control consists of a duty cycle in current limited mode. In the previous section, it is demonstrated that the minimal current to heat the thruster to its MOT, I_{stat}, determines a heating time on the order of hours. This is not compatible with the mission requirements shown in Table 2. Consequently, higher current, hence power, is necessary to reach the MOT within the anticipated heating time requirements. Once the operational temperature is reached, the heater must then switch off. Therefore, a pulse width operation is necessary to maintain the objective temperature and a duty cycle is determined.

In the following example, STAR-Inc is subjected to a pulsed width heating cycle with two test currents corresponding to about 25 W (I = 24.4 A) and 50 W (I = 34.2 A). A domain probe evaluates the maximum structural temperature, T_m. The heater switches on when the measured temperature falls below 90% of MOT, while it switches off when MOT is reached. Fig. 13 depicts the first 30 seconds of the simulation, showing the structural maximum temperature, the maximum stagnation temperature and the electrical current. The resulting duty cycles are D = 89% for P_e = 25 W and D = 42% for P_e = 50 W, which corresponds to an average power of 22.3 W and 21 W respectively. In the first case, the peak stagnation temperature rises from 1146 K to 1149 K, while in the second case from 1108 K to 1150 K during the two minutes of simulation. In the stationary case, corresponding to a continuous application of I_{stat}, the stagnation temperature reaches 1253 K. The selection of the power control depends uniquely on the PPU constraints, which is not subject to this work.

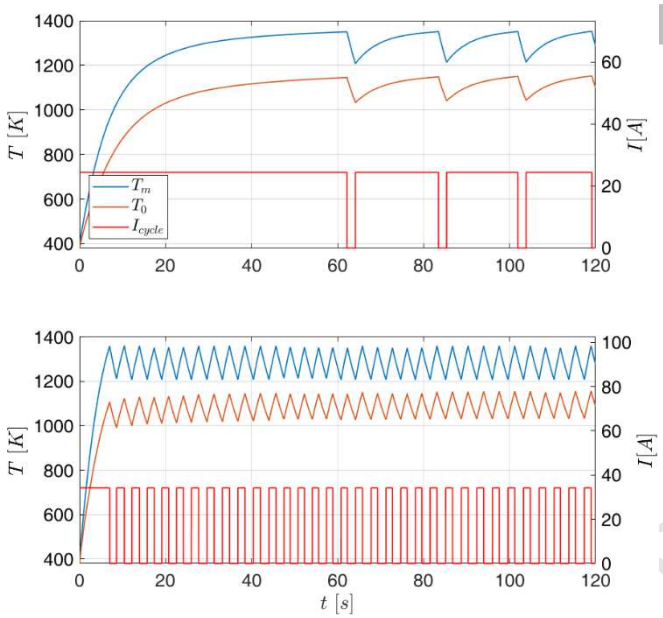

Fig. 13. Pulse-width heating cycle of STAR-Inc with two current levels corresponding to approximately 25 W and 50 W of electrical power.

3.4.3 Results

The heat exchanger efficiency in combination with the nozzle efficiency provides the total thruster efficiency, η_{ts}, as shown by Eq.(17). Table 7 compares the specific impulse, total thruster efficiency, electric power and difference between the maximum structural and the stagnation temperatures, ΔT, calculated in the time-dependent and the stationary cases. The time-dependent cases correspond to the maximum currents evaluated for each thruster in Section 3.4.1, where t_h is the heating time necessary to reach the MOT.

$$h_{ts} = h_h h_n \tag{17}$$

Table 7. Comparison between performance immediately after ignition and the maximum performance achievable corresponding to the stationary solution.

Parameter	STAR-Inc		STAR-Ta		STAR-Re	
	t_h = 8.2 s	t ® ¥	t_h = 35.1 s	t ® ¥	t_h = 51.1 s	t ® ¥
I_{sp} [s]	56.4	59.9	83.5	85.0	86.7	87.7
h_{ts} [%]	26.8%	62.0%	41.3%	58.2%	45.9%	55.1%
P_e [W]	49.4	13.3	512.4	277.6	477.8	310.8
DT [K]	239.8	95.6	206.8	131.5	183.5	91.5

4. Conclusions

In the three cases analysed, the temperature obtainable within one minute is close to the maximum operating temperature evaluated with the stationary solution. In particular, $I_{sp}(t_h)/I_{sp}(\infty)$ results in 94%, 98% and 99% for the three thrusters respectively. Therefore, $I_{sp}(\infty)$ could be obtained within minutes using a high-current heat-up, followed by a lower current firing mode, aimed at maintaining the operational temperature. It has to be noted that the thruster dimensioning, including thermal insulation and radiation shielding selection, was not subjected to an optimisation process. Rather, this paper explores the STAR design in the three exploratory cases of interest. A detailed design of the STAR resistojet should aim to increase the thruster efficiency in the region of 70%.

A high-temperature resistojet would provide a significant increase in fuel efficiency with respect to the currently available state of the art Xe-resistojets. In particular, two selected missions would benefit of this technology, M1, where the resistojet would be used as primary propulsion system in small LEO platforms and M2, where a number of thrusters would be used as RCS of all-electric GEO platforms. In this paper, the concept of the STAR thruster has been investigated using multiphysics simulations with three selected materials, namely Inconel 718, pure Ta and pure Re, with specific assumptions implemented on the geometry and

materials. A preliminary dimensioning of the nozzle at the requirements of the M1 mission immediately highlighted that, at extreme temperatures, the nozzle would have lower specific impulse efficiency. For this reason, STAR-Inc is selected for M1, while the extreme temperature thrusters, STAR-Ta and STAR-Re, are selected for M2. Steady-state studies provided the minimum current necessary to reach the operational temperature, while time-dependent studies provided the heating time at increasing current levels. In all cases, the objective temperature is reached within the start-up duration requirement. Finally, a heating cycle example on the STAR-Inc shows a possible mode of operation at constant current, which results in a quasi-constant duty cycle.

Acknowledgements

This research was funded by the Doctoral Training Partnership through the Engineering and Physical Sciences Research Council (EPSRC), grant no. EP/M50662X/1. All data supporting this study are openly available from the University of Southampton repository at https://doi.org/10.5258/SOTON/D0633. The mission requirements were supplied by Surrey Satellite Technology Ltd as an end-user of the technology within the NSTP-2 High-Performance Xenon Resistojet project.

References

[1] A. N. Grubisic and S. B. Gabriel, "Assessment of the T5 and T6 Hollow Cathodes as Reaction Control Thrusters," *Journal of Propulsion and Power*, vol. 32, no. 4, pp. 810-820, 2016.

[2] M. Coletti, A. Grubisic, C. Collingwood, and S. Gabriel, "Electric propulsion subsystem architecture for an all-electric spacecraft," in *Advances in Spacecraft Technologies*, 2011, pp. 123-138.

[3] D. Gibbon, I. Coxhill, and M. Drube, "The Design, Build Test and In-Orbit Performance of the Giove-A Propulsion System," presented at the 5th International Spacecraft Propulsion Conference, Crete, 2008.

[4] I. G. Coxhill and D. Gibbon, "A Xenon Resistojet Propulsion System for Microsatellites," presented at the 41st AIAA/ASME/SAE/ASEE Joint Propulsion Conference & Exhibit, 10-13 July, 2005.

[5] F. Romei, A. N. Grubišić, and D. Gibbon, "Manufacturing of a high-temperature resistojet heat exchanger by selective laser melting," *Acta Astronaut.*, vol. 138, pp. 356-368, 9// 2017.

[6] F. Romei, A. Grubisic, and D. Gibbon, "High performance resistojet thruster: STAR Status Update," presented at the Space Propulsion Conference *2018, Seville, Spain, 14 - 18 May 2018*.

[7] M. Robinson *et al.*, "Endurance testing of the STAR additively manufactured resistojet," presented at the Space Propulsion Conference, Seville, Spain, 2018.

[8] C. Ogunlesi *et al.*, "Novel non-destructive inspection of the STAR additively manufactured resistojet," presented at the Space Propulsion Conference, Seville, Spain, 2018.

[9] R. G. Jahn, *Physics of Electric Propulsion*, 2006 ed. New York: Dover, 1968.

[10] C. R. Halbach, R. J. Page, and R. A. Short, "3-KW Concentric Tubular Resistojet Performance," *J Spacecraft Rockets*, vol. 3, no. 11, pp. 1669-1674, 1966.

[11] R. J. Page and R. A. Short, "Ten-Millipound Resistojet Performance," *J. SPACECRAFT*, vol. 5, no. 7, pp. 857-858, 1968.

[12] R. J. Page and R. A. Short, "Design of High-Performance Resistojets for Advanced Spacecraft," presented at the 9th Aerospace Sciences Meeting-Separate Papers - AIAA, 1971.

[13] J. Donovan and W. Lord, "Performance Testing of a 3kW Hydrogen Resistojet," DTIC Document, 1973.

[14] J. A. Donovan, W. T. Lord, and P. J. Sherwood, "Fabrication and Preliminary Testing of a 3kW Hydrogen Resistojet," presented at the The AIAA 9th Electric Propulsion Conference, 1972.

[15] (2016). *International Journal of Refractory Metals and Hard Materials* [Online]. Available: http://www.journals.elsevier.com/international-journal-of-refractory-metals-and-hard-materials/.

[16] Datasheet: Inconel alloy 718. [Online] Available: http://www.specialmetals.com/

[17] C. Y. Ho and T. Chu, "Electrical resistivity and thermal conductivity of nine selected AISI stainless steels," DTIC Document, 1977.

[18] P. D. Desai, T. Chu, H. M. James, and C. Ho, "Electrical resistivity of selected elements," *Journal of physical and chemical reference data*, vol. 13, no. 4, pp. 1069-1096, 1984.

[19] K. A. Polzin *et al.*, "Propulsion system development for the iodine satellite (iSAT) demonstration mission," 2015.

[20] K. A. Polzin, J. F. Seixal, S. L. Mauro, A. O. Burt, A. Martinez, and A. K. Martin, "The iodine Satellite (iSat) Propellant Feed System-Design and Development," presented at the International Electric Propulsion Conference, Atlanta, 2017.

[21] S. Mazouffre, "Electric propulsion for satellites and spacecraft: established technologies and novel approaches," *Plasma Sources Science and Technology*, vol. 25, no. 3, p. 033002, 2016.

[22] P. Sherwood, "Construction of a High Performance Resistojet for Satellite Propulsion," DTIC Document, 1978.

[23] E. Bich, J. Millat, and E. Vogel, "The viscosity and thermal conductivity of pure monatomic gases from their normal boiling point up to 5000 K in the limit of zero density and at 0.101325 MPa," *Journal of physical and chemical reference data*, vol. 19, no. 6, pp. 1289-1305, 1990.

[24] S. C. Kim, "Calculations of Low-Reynolds-Number Resistojet Nozzles," (in English), *J Spacecraft Rockets*, vol. 31, no. 2, pp. 259-264, Mar-Apr 1994.

[25] A. D. Ketsdever, M. T. Clabough, S. F. Gimelshein, and A. Alexeenko, "Experimental and numerical determination of micropropulsion device efficiencies at low reynolds numbers," (in English), *AIAA Journal*, Article vol. 43, no. 3, pp. 633-641, 03 / 01 / 2005.

[26] M. M. Hussaini and J. J. Korte, "Investigation of low-Reynolds-number rocket nozzle design using PNS-based optimization procedure," in "TM110295," NASA, 1996.

[27] M. V. Whalen, "Low Reynolds number nozzle flow study," in "TM100130," NASA, 1987.

[28] *CFD Module User's Guide*: COMSOL 5.3, 2017.

[29] Promat. Datasheet: Promalight - High Temperature Microporous Insulation Board [Online] Available: http://www.promat-hpi.com/

[30] Product Data Book [Online] Available: http://www.morganadvancedmaterials.com

Paper highlights:

- A novel high-temperature resistojet design enables all-electric spacecraft;
- A numerical study predicts transient and steady state performance characteristics;
- Specific impulse > 80 s with Xe is achievable with Ta or Re heat exchangers;
- Specific impulse up to 60 s with Xe is achievable with an Inconel heat exchanger;
- In all examined cases, the resistojet reaches the maximum performance in < 1 minute;